

DMRVisNet: Deep Multi-head Regression Network for Pixel-wise Visibility Estimation Under Foggy Weather

Jing YOU*, Shaocheng JIA*, Xin PEI, and Danya YAO

Abstract—Scene perception is essential for driving decision-making and traffic safety. However, fog, as a kind of common weather, frequently appears in the real world, especially in the mountain areas, making it difficult to accurately observe the surrounding environments. Therefore, precisely estimating the visibility under foggy weather can significantly benefit traffic management and safety. To address this, most current methods use professional instruments outfitted at fixed locations on the roads to perform the visibility measurement; these methods are expensive and less flexible. In this paper, we propose an innovative end-to-end convolutional neural network framework to estimate the visibility leveraging Koschmieder’s law exclusively using the image data. The proposed method estimates the visibility by integrating the physical model into the proposed framework, instead of directly predicting the visibility value via the convolutional neural work. Moreover, we estimate the visibility as a pixel-wise visibility map against those of previous visibility measurement methods which solely predict a single value for an entire image. Thus, the estimated result of our method is more informative, particularly in uneven fog scenarios, which can benefit to developing a more precise early warning system for foggy weather, thereby better protecting the intelligent transportation infrastructure systems and promoting its development. To validate the proposed framework, a virtual dataset, FACI, containing 3,000 foggy images in different concentrations, is collected using the AirSim platform. Detailed experiments show that the proposed method achieves performance competitive to those of state-of-the-art methods.

Index Terms—Visibility estimation, DMRVisNet, FACI dataset, Multi-task learning.

I. INTRODUCTION

VISIBILITY, as an important indicator in traffic management, is defined as the maximum horizontal distance at which a person with normal vision can recognize a black and moderately sized target object from the sky background by the World Meteorological Organization, International Commission

on Illumination (CIE), and American Meteorological Society [1]–[3]. According to the level of degradation, visibility is classified into 10 classes by the British Meteorological Service, in which the lowest level corresponds to heavy fog with visibility less than 50 meters while the highest level corresponds to the visibility greater than 30 kilometers [1].

Fog, as one of the most common contributing factors to low visibility, is defined as a kind of cloud on the ground and formed by the suspension of microscopic moisture dewdrops into airborne particles [4]. The low visibility caused by foggy weather will lead to various consequences. For instance, low visibility will pose a threat to traffic safety by making it difficult for drivers to perceive the driving environment and further make driving decisions [4]–[7]. Previous studies have validated that the traffic accident rate strikingly increases when the visibility is less than 200 meters [8], even the fatal multi-vehicle pileups [5], [9]. More specifically, approximately 30% of fatal crashes were related to fog in the USA from 1990 to 2012 and almost two-thirds of them led to serial collisions involving 10 or more vehicles [10]. These crashes can heavily damage the transportation infrastructure systems. Moreover, visibility is also correlated with flight safety [11]–[13], image quality [14], [15], air quality [16], [17], even economy [18]–[20].

Apart from the transportation infrastructure systems probably being damaged by the low visibility-induced accidents, some equipment and sensors might also be affected by the low visibility weather, such as camera and Light Detection And Ranging (LiDAR)). Thus, obtaining accurate visibility information can protect the transportation infrastructure systems, as well as promote the development of intelligent transportation infrastructure systems.

To this end, it is necessary to precisely estimate the visibility under foggy weather. However, it is extremely challenging because (1) visibility is a rather complex parameter and influenced by many atmospheric conditions, such as light scatter, air light, and light absorption; (2) using a single value to represent visibility is difficult unless the fog is uniform across the whole image, which occurs rarely in reality [1], [5]. Still, the earliest literature concerning visibility estimation can date back to the 1920s when Koschmieder’s law [21], a fundamental theory for atmospheric visibility estimation, was proposed. Following that, tons of work has been done using different methods, including the traditional methods, the statistical methods, and the recent deep neural network (DNN) methods.

* Contributed equally.

This work has been submitted to the IEEE for possible publication. Copyright may be transferred without notice, after which this version may no longer be accessible. The work described in this paper was supported by the National Key Research and Development Program of China (Grant No. 2021YFC3001501) and the National Natural Science Foundation of China (Grant No. 71671100). (Corresponding author: Xin PEI)

Jing YOU is with the Department of Automation, Tsinghua University, Beijing, China; Shaocheng JIA is with the Department of Civil Engineering, The University of Hong Kong, Hong Kong, China; Xin PEI is with the Department of Automation, Beijing National Research Center for Information Science and Technology, Tsinghua University, Beijing, China; Danya YAO is with the Department of Automation, Beijing National Research Center for Information Science and Technology, Tsinghua University, Beijing, China.

Traditional methods adopt either manual observations or professional instruments. For observations, the result may change from observer to observer; For professional instruments, they are costly and less flexible [4], [9]. By contrast, the statistical methods estimate the visibility from the collected data using either the definition or the relationship between the visibility and the data. These methods also require geographic calibration or solely can be used in some special cases. Recently, Some researchers applied DNN models to performing visibility estimation. However, DNN models require large-scale datasets for training, while collecting data from real-world situations is time-consuming and expensive. Importantly, solely using DNN models to estimate the visibility in an end-to-end manner is difficult to interpret how the models work [1], [22], [23]. Additionally, publicly available visibility estimation datasets are very rare because collecting visibility data in the real world is time-consuming and costly, which hinders the development of visibility estimation methods.

To tackle the aforementioned issues, we propose a novel multi-head regression convolutional neural networks (CNN) framework, DMRVisNet, which integrates the physical laws and the deep learning methods to estimate the physical parameters in Koschmieder's law [21] instead of directly predicting visibility. Moreover, the proposed method outputs a visibility map, for which it is more robust and informative under uneven fog situations. To validate the proposed method, a virtual dataset, Foggy Airsim City Images (FACI) is collected using the Airsim simulation platform [24].

To sum up, our contributions are as follows:

- We propose a novel multi-head regression convolutional neural network framework, DMRVisNet, to estimate visibility by integrating the physical laws and the deep learning methods;
- We propose a new pixel-wise visibility estimation paradigm, which is more informative and practical, particularly in uneven fog scenarios;
- We propose a new virtual dataset, FACI, to be used for both pixel-wise and single-value visibility estimation (it will be publicly available once the paper is accepted).
- The proposed method achieves performance competitive compared to those of state-of-the-art methods.

The remainder of this paper is organized as follows. Section II introduces related works. Section III mathematically defines the problem and presents notational conventions. Section IV presents the proposed dataset, model, and loss functions. Section V reports on detailed experiments. Section VI discusses the limitations of the proposed model. Section VII draws the conclusions.

II. RELATED WORK

In this section, we review the literature related to visibility estimation, which is divided into 3 categories: the traditional methods, the statistical methods, and the methods based on DNNs.

A. Traditional methods

Traditional methods mainly consist of two types of estimation paradigms, i.e., manual observation and professional

instruments. For the former, the estimation accuracy heavily depends on the observer. For the latter, professional instruments (e.g., scatterometers, transmissometers, and Light Detection And Ranging (LiDAR)) are first used for measuring the environmental parameters, such as extinction coefficient and the transmission, then the Koschmieder's law [21] is used for visibility estimation. These professional instruments are comparatively precise, yet they are costly and require specialized installation and calibration. Accordingly, professional instruments are solely used in some special cases [4], [9], such as fixed-location meteorological stations.

B. Statistical methods

Statistical methods also can be roughly divided into two estimation paradigms, i.e., estimation by definition and correlation between visibility and feature respectively, and both of them are data-driven methods. For definition estimation, it is to estimate the farthest visible object in the scene. For example, Pomerleau et al. detected lane lines in the image captured by the on-board camera and then estimated visibility leveraging the attenuation of contrast [9]. For correlation estimation, it is to discover the underlying relationship between visibility and features extracted from source data (e.g., images). For instance, Hallowell et al. attempted to find the relationship between visibility and edge attenuation using the images captured by the fixed-position camera in sunny weather [25]. Following that, so many works have been done in improving either feature extraction or correlation function [6], [19], [26]–[32].

Statistical methods are much more convenient than traditional methods. However, most statistical methods require either geographic calibration or special scenarios to be used, which hinders statistical methods being widely used.

C. Methods based on DNNs

Recent performance advances in a variety of computer vision tasks are own to the development of deep neural networks to great extent. Thus, there are also so many trials applying the DNNs to Visibility estimation. In 1995, multilayer perceptron (MLP) was first introduced to perform visibility estimation [33]. Following that, several MLP-based methods were introduced [4], [34]. Representatively, the risk neural network was proposed to accommodate the basic principle that low visibility should have a higher risk value for the same forecast error [34], which improved the performance of the standard MLP method.

Thereafter, convolutional neural networks (CNNs) were prevalent because of their excellent performance in image processing. Therefore, tremendous work has been conducted by introducing CNNs in visibility estimation [1], [20], [22], [23], [35]. In these methods, CNNs are used to either extract features from the input images or learn the correlations between the features and visibility. Additionally, the abundant features of multimodal data (e.g., ordinary camera and infrared camera) were used to improve the performance of visibility estimation as well [36]. However, few of them consider

integrating the physical laws for better interpretation and performance improvement.

In summary, traditional methods have solid mathematical foundations but are very difficult to be widely used taking the capital cost and flexibility into account. Statistical methods are early explorations of the data-driven paradigm. Current deep neural network methods are capable of extracting the deep and abstract features from the raw data, but lack interpretability. To the best of our knowledge, none of the work attempts to integrate the physical laws and deep learning methods; none of the work proposes pixel-wise visibility estimation paradigm, either, however, which is significant for uneven fog cases. These issues motivate us to conduct this work.

III. PROBLEM SETUP

Our pixel-wise visibility estimation system Ψ comprises three parts, namely the airlight estimation network, the transmission estimation network, and the depth estimation network, denoted as Ψ_A , Ψ_T , and Ψ_D , respectively. Given an image I , the airlight estimation network Ψ_A solely takes the input image I as the input to predict its airlight; this can be mathematically defined as: $\Psi_A : I \in \mathbb{R}^{h \times w \times c} \rightarrow A \in \mathbb{R}^3$, where A , h , and w are the predicted airlight of the input image I , the height of the input image, and the width of the input image, respectively. Similarly, the transmission estimation network Ψ_T takes the input image I as the input to predict its transmission map; this can be mathematically defined as: $\Psi_T : I \in \mathbb{R}^{h \times w \times c} \rightarrow T \in \mathbb{R}^{h \times w}$, where T is the predicted transmission map of the input image I . To make the network easier to be optimized, Ψ_D , which is used to estimate the depth map, will take the input image I as input and output the disparity map \bar{D} , i.e. $1 \oslash D$, where D and \oslash represent the predicted depth map of the input image I and element-wise division, respectively; this can be mathematically defined as: $\Psi_D : I \in \mathbb{R}^{h \times w \times c} \rightarrow \bar{D} \in \mathbb{R}^{h \times w}$.

Theoretically, given the transmission map and depth map of the input image, the pixel-wise visibility map can be calculated by Koschmieder's law [21], which is mathematically defined as Eq. 1.

$$V = \ln(\epsilon) \otimes D \oslash \ln(T), \quad (1)$$

where $V \in \mathbb{R}^{h \times w}$ and \otimes represent the visibility map and element-wise multiplication respectively; ϵ is the threshold defined by the International Commission on Illumination (CIE) to describe the meteorological visibility distance. Note that the airlight A is used to train the model as an aid, though it is not shown in the Eq. 1.

IV. METHOD

In this section, visibility estimation theories used for generating the FACI dataset and designing DMRVisNet are first introduced. Subsequently, FACI dataset and DMRVisNet are introduced, respectively. Finally, the loss functions used in this paper are presented.

A. Visibility estimation

The intensity of the light will gradually decrease along with the increase of the distance due to the scattering, refraction, and other physical phenomena. In reality, we can find that the luminance of the further object is weaker than that of the closer one, even they have exactly identical luminance in fact. This phenomenon can be mathematically described as Eq. 2 [21].

$$\begin{aligned} \hat{I} &= \hat{J}\hat{T} + \hat{A}(1 - \hat{T}) \\ \hat{T} &= e^{-\hat{\beta}\hat{D}}, \end{aligned} \quad (2)$$

wherein \hat{J} , \hat{I} , \hat{T} , \hat{A} , \hat{D} , and $\hat{\beta}$ represent the intrinsic luminance of the object, the observed luminance of the object, the transmission at the position of the object, the airlight (it results from daylight scattered by the slab of fog between the object and the observer), the depth of the object, and the extinction coefficient of the atmosphere, respectively.

According to Eq. 2, we can learn that the observed luminance is the linear weighting between the intrinsic luminance and the airlight; the weighting factor, \hat{T} , decays exponentially against the product of the depth and the extinction coefficient.

Similarly, for a digital image, applying Eq. 2 we can readily deduce to Eq. 3.

$$\begin{aligned} I &= J \otimes T + A \otimes (1 - T) \\ T &= e^{\beta \otimes D}, \end{aligned} \quad (3)$$

where J , I , T , A , D , and β represent the fogless image, the foggy image, the transmission map, the airlight map, the depth map, and the extinction coefficient map, respectively. Generally, the airlight across the different positions in the image is regarded as constant [37]–[41]. Thus, the airlight map is single-valued.

To define the attenuation of the contrast, the definition of contrast is first introduced, being the relative luminance of the object compared to its background, which is stated in Eq. 4.

$$Con = \frac{Obj - Back}{Back}, \quad (4)$$

where Con , Obj , and $Back$ represent the contrast of the object, the luminance of the object, and the luminance of the background, respectively.

Therefore, consolidating Eq. 2 and Eq. 4 we can readily derive to the attenuation of the contrast [42], which can be described as 5.

$$\begin{aligned} C_J &= \frac{\hat{J} - \hat{A}}{\hat{A}} \\ C_{\hat{I}} &= C_J \hat{T}, \end{aligned} \quad (5)$$

similarly, C_J represents contrast between the intrinsic luminance of object and the airlight; $C_{\hat{I}}$ represents contrast between the observed luminance of the object and the airlight. Eq. 5 indicates that the contrast between the luminance of the object and the airlight decays exponentially against the product of the depth and the extinction coefficient as well.

Assuming that the object is black, i.e., $\hat{J} = 0$, thus, Eq. 5 can be rewritten as Eq. 6.

$$\begin{aligned} C_J &= \frac{0 - \hat{A}}{\hat{A}} = -1 \\ C_{\hat{I}} &= C_J \hat{T} = -T. \end{aligned} \quad (6)$$

TABLE I
DESCRIPTION OF DATA IN FOCI BEFORE AUGMENTATION

Type	Description
Scene	Fog-free image
DepthPerspective	Pixel-wise depth map, you get depth from camera using a projection ray that hits that pixel

If $|C_f| < \epsilon$ holds, this black object is considered as unrecognizable, wherein $|\cdot|$ represents absolute value function and ϵ is the threshold defined by the International Commission on Illumination (CIE) to describe the meteorological visibility distance, generally being 5%. Accordingly, if $|C_f| = \epsilon$, visibility \hat{V} is exactly equal to \hat{D} . On this basis, we can deduce to Eq. 7 from Eq. 2 and Eq. 6.

$$|C_f| = |-T| = |-e^{-\hat{\beta}\hat{D}}| = |-e^{-\hat{\beta}\hat{V}}| = e^{-\hat{\beta}\hat{V}} = \epsilon. \quad (7)$$

Applying logarithmic function Eq. 7 can be rewritten as Eq. 8.

$$-\hat{\beta}\hat{V} = \ln(\epsilon). \quad (8)$$

Similarly, applying logarithmic function to the second row of Eq. 2 we can deduce to Eq. 9.

$$\ln(\hat{T}) = -\hat{\beta}\hat{D}. \quad (9)$$

Consolidating Eq. 8 and Eq. 9, Eq. 10 is finally obtained for calculating visibility.

$$\hat{V} = \frac{-\ln(\epsilon)}{\hat{\beta}} = \frac{\ln(\epsilon)\hat{D}}{\ln(\hat{T})}. \quad (10)$$

Thus, Eq. 11 can be used to calculate the visibility map for an image.

$$V = \ln(\epsilon) \otimes D \oslash \ln(T), \quad (11)$$

where V , D , and T represent the visibility map, the depth map, and the transmission map, respectively. We can learn that visibility estimation can be converted to estimate the depth and transmission maps, which are relatively easier to be predicted. This will be used to devise the visibility estimation framework.

B. FOCI dataset

In this subsection, we first introduce the simulation platform Airsim [24] and its settings. Moreover, the details regarding the collected data are presented. Finally, the dataset's split is shown.

1) *Simulation platform*: AirSim [24] is an open-source and cross-platform simulator developed by Microsoft for Artificial Intelligence (AI) research, and supports software-in-the-loop simulation with popular flight controllers such as PX4 & ArduPilot and hardware-in-loop with PX4 for physically and visually realistic simulations; it can help experiment with deep learning, computer vision, and reinforcement learning algorithms, especially for autonomous vehicles.

During collection, Version 1.3.1 of AirSim is used on Windows; among the several maps provided by developers, a city scene is chosen; to make the cameras move more freely, the Computer Vision mode is used; and the height and width of the images are set to 576 and 1,024, respectively.

2) *Data details*: We collected 100 groups of original data in different scenes, and each group consists of fogless images and depth maps. The detailed descriptions regarding the dataset are shown in Table I and Figure 1.



Fig. 1. Illustration of the collected original data. (a) Fogless image. (b) Pixel-wise depth map, you get depth from camera using a projection ray that hits that pixel.

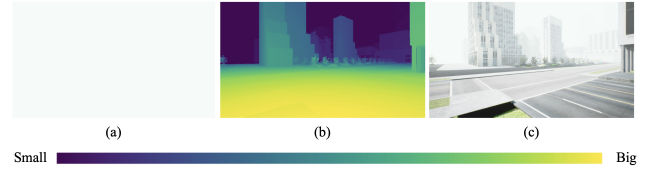


Fig. 2. Visualization of augmented data. (a) RGB value of airlight. (b) Pixel-wise transmission map. (c) Foggy image under current airlight and visibility map.

TABLE II
DESCRIPTION OF ADDITIONAL DATA IN FOCI AFTER AUGMENTATION

Type	Description
Visibility	Visibility value
A	RGB value of airlight
T	Pixel-wise transmission map
FoggyScene	Foggy image under current airlight and visibility map

Thereafter, we use the collected original data to generate the different foggy images. For each group of original data, 30 groups of augmented data are generated. The detailed procedure for generating a foggy image is described in Algorithm 1.

The detailed information after augmentation is shown in in Table II and Figure 2.

3) *data split*: FOCI dataset consists of 3,000 groups data, for which each group contains fogless image, depth map, visibility, airlight, transmission map under current visibility, foggy image under current airlight and visibility. We randomly divide 3,000 images into training set, validation set, and test set with respect to the ratio of 7:2:1, the number of sets of

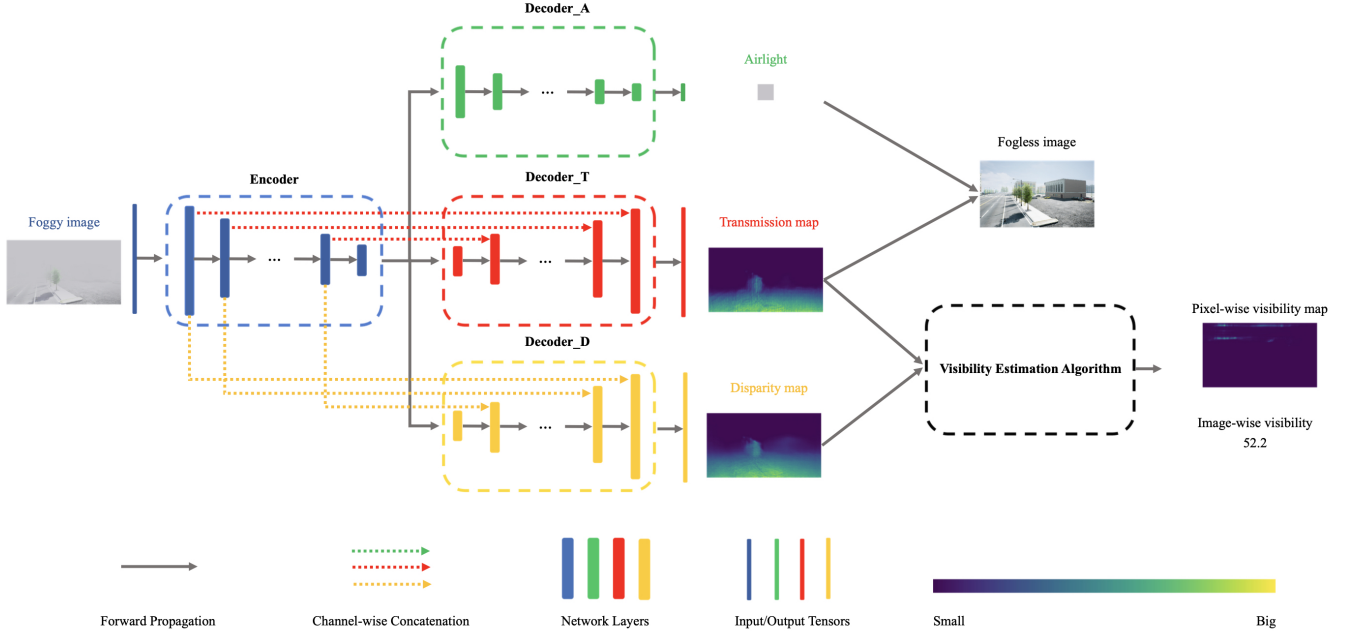


Fig. 3. DMRVisNet architecture. ResNet-18 [43] is adopted as encoder to extract features. Three separate decoders are used to estimate airlight, transmission map, and depth map respectively. Finally, the visibility estimation algorithm is used to couple the outputs to estimate the pixel-wise or image-wise visibility.

Algorithm 1 Generation of augmented data from original data

Input: The fogless image, J ; The depth map of fogless image, D ;

Output: The visibility map, V ; The airlight, A ; The transmission map, T ; The foggy image under this airlight and visibility map, I ;

- 1: To generate uniform fog, sample a value from the uniform distribution $U(10, 1000)$ (unit in meter) as the common value of visibility map V ;
- 2: Generate T with D and V according to Eq. 11;
- 3: Generate the red, green and blue (RGB) values of A , while the value of channel B is sampled from $U(180, 255)$, the value of channel G is sampled from $\min(U(B - 5, B + 2), 255)$ and the value of channel R is sampled from $\min(U(\frac{(B+G)}{2} - 5, \frac{(B+G)}{2} + 2), 255)$, to make the fog appear more real;
- 4: Generate I with J , A and T according to Eq. 3;
- 5: **return** V , A , T , I ;

data in training set, validation set and test set respectively is shown in Table III. Note that here are no overlapping scenarios between training set, validation set, and test set.

TABLE III

NUMBER OF SETS OF DATA IN TRAINING SET, VALIDATION SET AND TEST SET

Type	Number of sets of data
Training set	2100
Validation set	600
Test set	300

C. Model

Model overview. We propose a novel multi-head regression network, DMRVisNet, to simultaneously predict the airlight, the transmission map, and the depth map. Finally, the visibility estimation algorithm is used to couple the outputs, predicting the pixel-wise or image-wise visibility.

The architecture of DMRVisNet is shown in Figure 3, which consists of one encoder and three decoders, named by Encoder, Decoder_A, Decoder_T and Decoder_D, respectively.

Encoder. ResNet-18 [43] is adopted as encoder to extract multi-scale features. The architecture of the encoder is briefly illustrated in Figure 4, mathematically, which can be described as Eq. 12.

$$F = \text{Encoder}(I), \quad (12)$$

where F and I represent the features extracted from Encoder and the input image.

Decoders. Following Encoder, three separate decoders, i.e., Decoder_A, Decoder_T, and Decoder_D, are used to estimate airlight, transmission map, and depth map respectively, which can be described as Eq. 13.

$$\begin{aligned} \text{Decoder_A}(F) &= A_{est} \\ \text{Decoder_T}(F) &= T_{est} \\ \text{Decoder_D}(F) &= \bar{D}_{est}, \end{aligned} \quad (13)$$

where A_{est} , T_{est} , and \bar{D}_{est} represent the estimated airlight, the estimated transmission map and the estimated disparity map respectively. Thus, from an end-to-end manner, the airlight

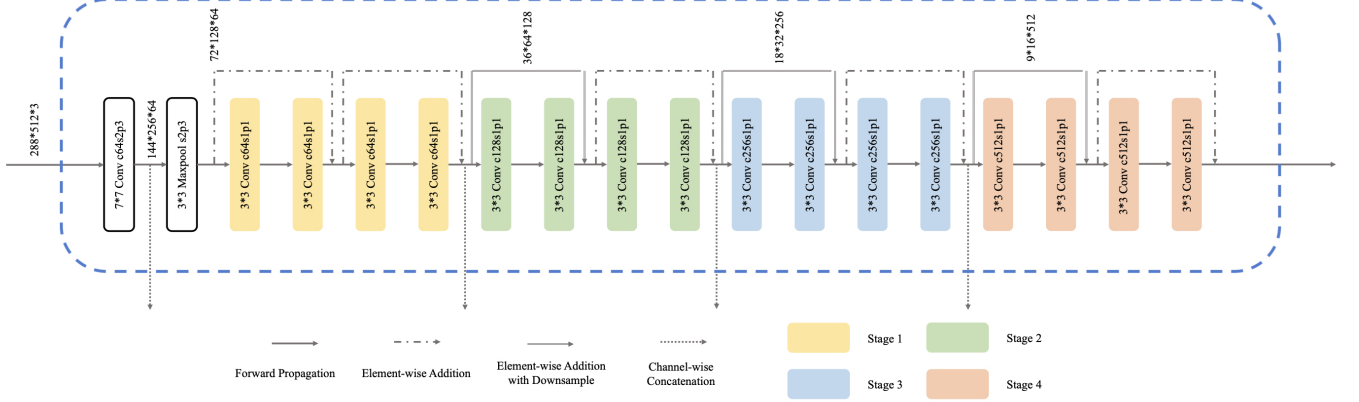


Fig. 4. Architecture of Encoder.

estimation, the transmission map estimation, and the disparity map estimation can be described as Eq 14.

$$\begin{aligned}\psi_A(I) &= \text{Decoder_A}(\text{Encoder}(I)) = A_{est} \\ \psi_T(I) &= \text{Decoder_T}(\text{Encoder}(I)) = T_{est} \\ \psi_D(I) &= \text{Decoder_D}(\text{Encoder}(I)) = \bar{D}_{est},\end{aligned}\quad (14)$$

where Ψ_A , Ψ_T , and Ψ_D represent the airlight estimation network, the transmission estimation network, and the depth estimation network, respectively.

For transmission map and disparity map estimation, a coarse-to-fine architecture used in Monodepth2 [44] is adopted, shown as Fig. 6. For airlight estimation, several CNN layers are used, shown as Fig. 5.

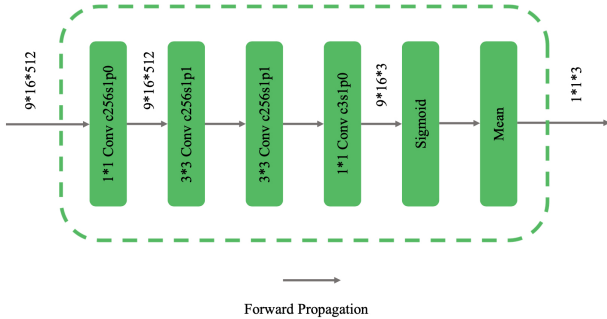


Fig. 5. Architecture of Decoder_A.

Thus, simply integrating encoder and decoders we can obtain the three results, i.e., airlight, which is used to obtain the estimated fogless image and consequently train the model; transmission map and depth map, which are the inputs of the visibility estimation algorithm.

Visibility estimation algorithm. According to Eq. 11, we can readily deduce to Eq. 16 for pixel-wise visibility estimation.

$$V_{est} = \ln(\epsilon) \otimes D_{est} \oslash \ln(T_{est}), \quad (16)$$

Algorithm 2 Visibility estimation algorithm

Input: The estimated transmission map, T_{est} ; The estimated depth map, D_{est} ; The lowest threshold of estimated transmission map \hat{T}_{min} ; The highest threshold of pixel-wise visibility map, \hat{V}_{max} ; The lowest threshold of pixel-wise visibility map, \hat{V}_{min} ;

Output: The estimated pixel-wise visibility map, V_{est} ; The estimated image-wise visibility, \hat{V}_{est} ;

- 1: Generate V_{est} with T_{est} and D_{est} according to Eq. 16;
- 2: Generate \hat{V}_{est} with V_{est} and T_{est} according to Eq. 15;

$$\hat{V}_{est} = \begin{cases} \frac{\text{SUM}(V_{est} \otimes \text{mask})}{\text{SUM}(\text{mask})}, & \text{if } \text{SUM}(\text{mask}) \neq 0 \\ \hat{V}_{min}, & \text{otherwise} \end{cases}$$

$$\text{mask} = \text{MASK}(\hat{T}_{min}, T_{est}) \otimes \text{MASK}(-\hat{V}_{max}, -V_{est})$$

$$\text{MASK}(t, \text{mat})(i, j) = \begin{cases} 1, & \text{if } \text{mat}(i, j) > t \\ 0, & \text{otherwise} \end{cases}$$

$$\text{SUM}(\text{mat}) = \sum_i^h \sum_j^w \text{mat}(i, j),$$

(15)

where MASK is a function defined as $\text{MASK} : t \times \text{mat} \in \mathbb{R} \times \mathbb{R}^{h \times w} \rightarrow \mathbb{R}^{h \times w}$ and SUM is a function defined as: $\text{SUM} : \text{mat} \in \mathbb{R}^{h \times w} \rightarrow \mathbb{R}$. Moreover, i, j, h, w represent the row index, the column index, the height and the width of the input matrix mat , respectively.

- 3: **return** V_{est}, \hat{V}_{est} ;

where V_{est} , D_{est} and T_{est} represent estimated visibility map, estimated depth map and estimated transmission map, respectively.

To compare with other methods, we also convert pixel-wise visibility to image-wise visibility based on the followings: (1) not every pixel in the visibility map is valid, e.g. pixels in sky area, in which the transmission \hat{T} is 0, the depth \hat{D} is infinity, and the visibility \hat{V} can not be calculated from Eq. 10; and (2) some extremely large outliers in visibility map should be ignored due to the limited human vision. Thus, we calculate

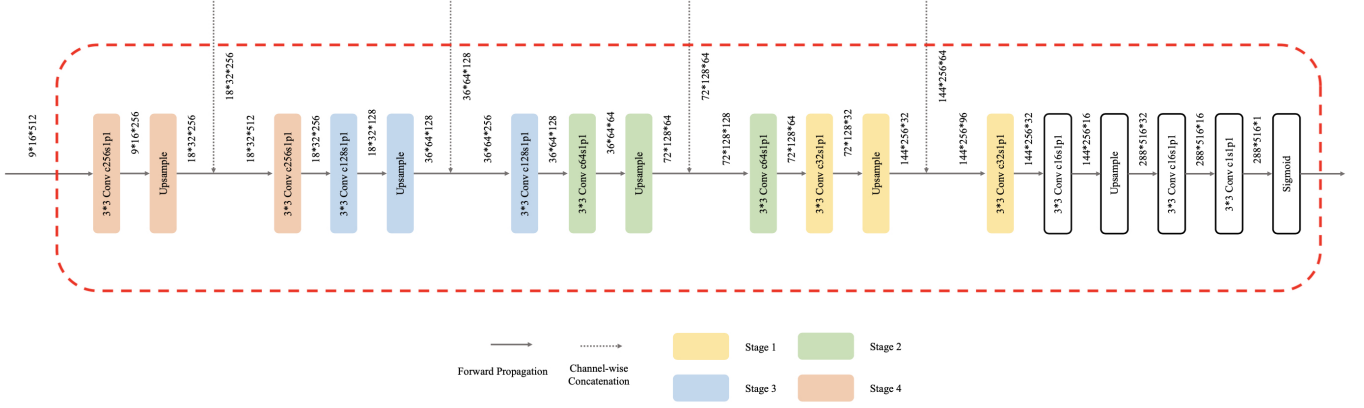


Fig. 6. Architecture of Decoder_T and Decoder_D.

the mean value of the visibility map where the transmission is greater than the threshold \hat{T}_{min} and the estimated visibility is lower than the maximum visibility \hat{V}_{max} . If the number of valid pixels in estimated visibility map is 0, the visibility is set to the minimum value \hat{V}_{min} , which is 10 meters for the FACI dataset. The detailed procedure for visibility estimation algorithm is described in Algorithm 2.

D. Losses

In this subsection, the loss functions used to train the framework are presented. As presented in Section IV-C, the proposed framework first performs multi-task learning, then multiple results are coupled with Koschmieder's law [21]. Thus, the loss functions for different tasks work together to train the network, which is shown in Eq. 17.

$$L = \lambda_A L_A + \lambda_T L_T + \lambda_D L_D + \lambda_{defog} L_{defog} + \lambda_{vis} L_{vis}, \quad (17)$$

wherein L , L_A , L_T , L_D , L_{defog} , and L_{vis} represent the final loss function, the loss for airlight estimation, the loss for transmission map estimation, the loss for fogless image estimation, and the loss for visibility estimation, respectively; λ_A , λ_T , λ_D , λ_{defog} , and λ_{vis} are hyperparameters. In what follows, the detailed definition of each term in Eq. 17 is presented.

1) L_A : Root mean square error (RMSE) loss is used for airlight estimation, which can be stated in Eq. 18.

$$L_A = \|A_{est} - A\|_2, \quad (18)$$

where A_{est} represents the estimated airlight, which is derived from the airlight estimation network Ψ_A as Eq. 14.

2) L_T : Root mean square error (RMSE) loss is also used for transmission map estimation, which can be stated in Eq. 19.

$$L_T = \|T_{est} - T\|_2, \quad (19)$$

where T_{est} represents the estimated transmission map, which is derived from the transmission estimation network Ψ_T as Eq. 14.

3) L_D : Following Jia et al. [45], we use the combination of L1 Loss, Structure Similarity (SSIM) Loss [46], and Smoothness Loss as L_d to train the disparity estimation head, which is stated in Eq. 20.

$$\begin{aligned} L_D = & \lambda_{L1} \|\bar{D}_{est} - \bar{D}\|_1 \\ & + \lambda_{SSIM} \frac{1 - SSIM(\bar{D}_{est}, \bar{D})}{2} \\ & + \lambda_{Smooth} \frac{\text{SUM}(|e^{-\partial_x(J)}| \otimes \partial_x(\bar{D}_{est}))}{h * w} \\ & + \lambda_{Smooth} \frac{\text{SUM}(|e^{-\partial_y(J)}| \otimes \partial_y(\bar{D}_{est}))}{h * w}, \end{aligned} \quad (20)$$

where ∂ , \bar{D} , \bar{D}_{est} , h , w and J represent the gradient operator, the disparity map, the estimated disparity map, the height of estimated disparity map, the width of estimated disparity map and the fog-free color image, respectively; λ_{L1} , λ_{SSIM} , and λ_{Smooth} are hyperparameters.

Following Jia et al. [45], the hyperparameters mentioned above are set as follows: $\lambda_{L1} = 0.15$, $\lambda_{SSIM} = 0.85$, and $\lambda_{Smooth} = 1e - 3$.

4) L_{defog} : According to Eq. 3, the defogged image J can be obtained from Eq. 21.

$$J = (I - A) \otimes T + A, \quad (21)$$

where I , A , and T represent the foggy image, the airlight and the transmission map, respectively.

Consequently, the estimated fogless image J_{est} can be obtained from Eq. 22.

$$J_{est} = (I - A_{est}) \otimes T_{est} + A. \quad (22)$$

Then, RMSE loss is used to train the defogging head. This can be mathematically defined as Eq. 23.

$$L_{defog} = \|J_{est} - J\|_2. \quad (23)$$

5) L_{vis} : Eq. 11, which is used to calculate visibility map V , can be rewritten as Eq. 24.

$$V = \ln(\epsilon) \otimes (\bar{D} \otimes \ln(T)). \quad (24)$$

The estimated visibility map V_{est} can be derived from Eq. 25.

$$\begin{aligned} V_{est} &= \ln(\epsilon) \otimes (\bar{D}_{est} \otimes \ln(T_{est})) \\ &= \ln(\epsilon) \otimes (\Psi_D(I) \otimes \ln(\Psi_T(I))). \end{aligned} \quad (25)$$

Note that $\ln(\epsilon)$ is constant, we solely constrain $\Psi_D(I) \otimes \ln(\Psi_T(I))$. To achieve this, L1 Loss is used, which can be defined as Eq. 26.

$$L_{vis} = \|\bar{D}_{est} \otimes \ln(T_{est}) - \bar{D} \otimes \ln(T)\|_1. \quad (26)$$

V. EXPERIMENTS

In this section, we first introduce the implementation details. Then the results and comparisons with other state-of-the-art methods are showed. Thereafter, the parameter analysis, ablation studies and model complexities are presented, respectively.

A. Implementation details

Experimental environment. All experiments were conducted with PyTorch 1.6.0 [47] on Ubuntu 16.04.6 LTS. The detailed information is shown in Table IV.

TABLE IV
EXPERIMENTAL ENVIRONMENT

Item	Content
CPU	Intel Core i7-6900K CPU @ 3.20GHz
GPU	NVIDIA GeForce GTX 1080
RAM	128 GB
Operating System	Ubuntu 16.04.6 LTS
Programming Language	Python 3.8.3
Deep Learning Framework	Pytorch [47] 1.6.0
CUDA Version	CUDA 10.1

Data augmentation. During training phase, the image and corresponding pixel-wise labels are resized to 288×512 . Following Jia et al. [45], we perform data augmentations as follows: randomly cropping with relative size ranging from 0.75 to 1, random horizontal flips with a 50 percent chance, as well as random brightness, contrast, saturation, and hue jitter, with respective ranges of ± 0.2 , ± 0.2 , ± 0.2 , and ± 0.1 .

Hyperparameters. In training phase, we use Adam optimizer [48] with initial learning rate of $1e-5$ and batch size of 16. We multiply the learning rate by 0.1 when the fluctuations of L on validation set are less than $1e-4$ for 10 epochs, until the learning rate drops to $1e-8$. We train DMRVisNet for 300 epochs on a single GeForce GTX 1080 card, and the training process takes about 6 hours.

B. Results comparison

1) *Metrics:* For pixel-wise visibility estimation, we use absolute relative error (AbsRel), square relative error (SqRel), root mean square error (RMSE), and root mean square error (RMSElog) as metrics in our experiments. Their definitions are shown in Eq. 27, Eq. 28, Eq. 29, and Eq. 30; where y_{pred} , y_{gt} , and n represent the predicted value, ground truth and the number of valid pixels, respectively.

$$\text{AbsRel} = \frac{1}{n} \sum \left| \frac{y_{pred} - y_{gt}}{y_{gt}} \right|. \quad (27)$$

$$\text{SqRel} = \frac{1}{n} \sum \left(\frac{y_{pred} - y_{gt}}{y_{gt}} \right)^2. \quad (28)$$

$$\text{RMSE} = \sqrt{\frac{1}{n} \sum (y_{pred} - y_{gt})^2}. \quad (29)$$

$$\text{RMSElog} = \sqrt{\frac{1}{n} \sum (\log_{10}(y_{pred}) - \log_{10}(y_{gt}))^2}. \quad (30)$$

Generally, AbsRel is less than 20%, the estimated result is acceptable [32].

For image-wise visibility estimation, we use accuracy as the metric. To convert the regression results to classification results, we divide visibility into 5 classes, and each class and its corresponding visibility range are shown in Table V. Thus, the continuous outputs can be converted to different classes. The definition of accuracy is shown in Eq. 31.

$$\begin{aligned} \text{Accuracy} &= \frac{1}{n} \sum \mathcal{I}_{\text{CLASS}(y_{pred}) \doteq \text{CLASS}(y_{gt})} \\ \text{CLASS}(y) &= \begin{cases} 0, & \text{if } y < 200 \\ 1, & \text{if } 200 \leq y < 400 \\ 2, & \text{if } 400 \leq y < 600 \\ 3, & \text{if } 600 \leq y < 800 \\ 4, & \text{if } 800 \leq y \end{cases}, \end{aligned} \quad (31)$$

where CLASS is a function defined as: $\text{CLASS} : y \in \mathbb{R} \rightarrow \mathbb{Z}$, \mathcal{I} and \doteq represent indicator function and equivalence relation, respectively.

TABLE V
CLASS NUMBER AND ITS CORRESPONDING VISIBILITY RANGE (UNIT IN METER)

Class number	Visibility Range
0	< 200
1	200-400
2	400-600
3	600-800
4	> 800

2) *Results:* For a fair comparison, we reproduce other state-of-the-art methods on our platform using the proposed FACI dataset. All experiments are with identical configurations and hyperparameters. For image-wise visibility classification methods, cross-entropy (CE) loss is used during training. By contrast, Table V is used for visibility regression methods. In this case, all methods are comparable.

Table VI shows the quantitative results of different methods. We can find that most methods are image-wise classification methods which cannot provide the detailed visibility information. GRNN method [20] is to predict a single continuous visibility value for the input image. However, it cannot sense the uneven fog situations. By contrast, the proposed method can predict a pixel-wise visibility map. To the best of our knowledge, our work is the first to propose the pixel-wise visibility estimation paradigm.

From the numbers presented in Table VI, we can learn that the proposed method outperforms other state-of-the-art

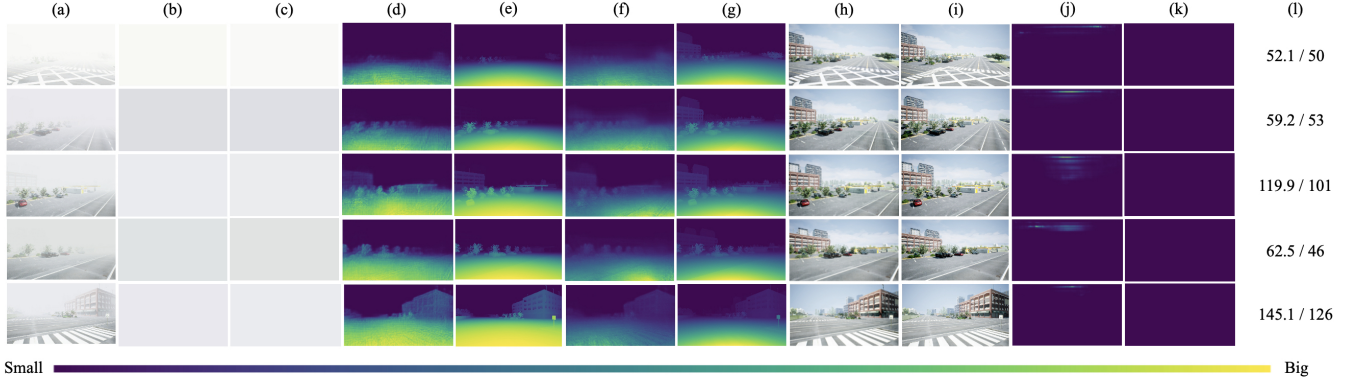


Fig. 7. Qualitative results on the test dataset. (a) The input images. (b) The estimated results of airlight. (c) The ground truths of airlight. (d) The estimated results of transmission map. (e) The ground truths of transmission map. (f) The estimated results of disparity map. (g) The ground truths of disparity map. (h) The estimated results of defog image. (i) The ground truths of defog image. (j) The estimated results of pixel-wise visibility map. (k) The ground truths of pixel-wise visibility map. (l) The estimated results of image-wise estimated visibility (left) and the ground truths of image-wise estimated visibility (right).

TABLE VI

QUANTITATIVE RESULTS OF THE VISIBILITY ESTIMATION ON THE FOCI DATASET. CLS AND REG REPRESENT CLASSIFICATION TASK AND REGRESSION TASK, RESPECTIVELY. THE BEST PERFORMANCES AND OUR MODEL ARE MARKED **BOLD**. THE SECOND BEST PERFORMANCES ARE UNDERLINED.

Methods	CLS?	REG?	Errors \uparrow		Errors \downarrow		
			Accuracy (unit in %)	AbsRel	SqRel	RMSE	RMSElog
PCASE [4]	✓	-	43.0	-	-	-	-
ResNet-50 [43]	✓	-	50.3	-	-	-	-
VGG-16 [49]	✓	-	<u>58.3</u>	-	-	-	-
VisNet [1]	✓	-	54.0	-	-	-	-
GRNN [20]	-	✓	54.3	0.27918	0.13469	156.59050	0.14024
Our	-	✓	68.3	0.17000	0.05094	93.11345	0.08429

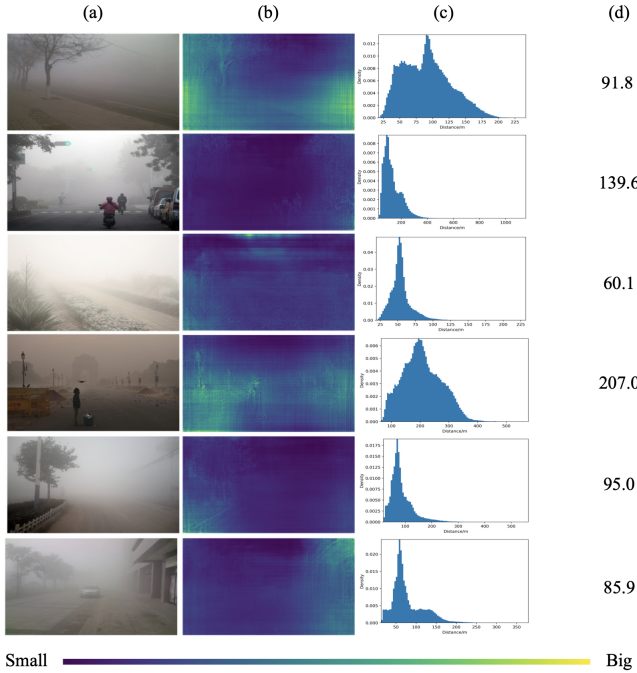


Fig. 8. Qualitative results on the real foggy images. (a) The input images. (b) The estimated results of pixel-wise visibility map. (c) The histograms of estimated pixel-wise visibility map. (d) The estimated results of image-wise visibility.

methods by large margins in all metrics. This demonstrates the effectiveness of the proposed framework.

Fig. 7 shows the qualitative results from the proposed method. We can learn that the proposed method can perform very well in different low-level vision tasks.

To further evaluate the practicality of the proposed method, we apply the model trained on the FOCI dataset to some real-world foggy images without any refinement. Fig. 8 presents the qualitative and quantitative results. We can learn that the proposed method can reflect the uniformity of fog from the visibility map or the histograms. For instance, the first and fourth images have uneven fog across different pixel positions, which has been clearly illustrated by the various intensities in visibility map and the bigger variances of the histograms.

To sum up, the quantitative and qualitative results demonstrate the effectiveness and advances of the proposed method. Some qualitative results on real-world data show the strong practicality of the proposed method.

C. Parameter analysis

In this subsection, we conduct some experiments to search for the most suitable set of hyperparameters.

Table VII shows the results under different λ_A , λ_T , λ_D , λ_{defog} , and λ_{vis} . The Control variable method is used to make the searching process achievable. As shown in Table VII, we manually set possible parameters for different hyperparameters

TABLE VII
PARAMETER ANALYSIS ON λ_A , λ_T , λ_D , λ_{defog} AND λ_{vis} . THE BEST PERFORMANCES ARE MARKED **BOLD**. THE SECOND BEST PERFORMANCES ARE UNDERLINED.

λ_A	λ_T	λ_D	λ_{defog}	λ_{vis}	Errors \uparrow	Errors \downarrow			
					Accuracy (unit in %)	AbsRel	SqRel	RMSE	RMSElog
0.6	1	1	$1e-6$	1	<u>66.0</u>	0.19477	0.06394	<u>111.68530</u>	0.09681
0.8	1	1	$1e-6$	1	<u>62.0</u>	<u>0.18804</u>	<u>0.05655</u>	<u>114.66917</u>	<u>0.09305</u>
1	1	1	$1e-6$	1	67.3	0.16662	0.04666	98.05333	0.08452
2	1	1	$1e-6$	1	63.7	0.23491	0.10370	128.72461	0.11392
3	1	1	$1e-6$	1	62.3	0.24748	0.10430	130.80329	0.11530
1	0.6	1	$1e-6$	1	<u>63.0</u>	0.25336	0.10989	132.24173	0.11595
1	0.8	1	$1e-6$	1	61.7	<u>0.18831</u>	<u>0.06276</u>	<u>109.26913</u>	<u>0.09434</u>
1	1	1	$1e-6$	1	67.3	0.16662	0.04666	98.05333	0.08452
1	2	1	$1e-6$	1	58.7	0.21396	0.07158	110.60130	0.09903
1	3	1	$1e-6$	1	16.7	0.96148	0.92773	565.60429	1.63656
1	1	0.6	$1e-6$	1	16.7	0.96148	0.92773	565.60429	1.63656
1	1	0.8	$1e-6$	1	68.3	<u>0.17000</u>	<u>0.05094</u>	93.11345	0.08429
1	1	1	$1e-6$	1	<u>67.3</u>	0.16662	0.04666	<u>98.05333</u>	<u>0.08452</u>
1	1	2	$1e-6$	1	62.3	0.20972	0.07609	115.81992	0.10196
1	1	3	$1e-6$	1	62.7	0.18594	0.06076	108.61163	0.09419
1	1	1	$1e-8$	1	61.7	0.20459	0.06836	<u>109.21708</u>	0.09732
1	1	1	$1e-7$	1	<u>64.3</u>	<u>0.19516</u>	<u>0.06514</u>	<u>119.81234</u>	<u>0.09489</u>
1	1	1	$1e-6$	1	67.3	0.16662	0.04666	98.05333	0.08452
1	1	1	$1e-5$	1	50.0	0.38631	0.23161	213.53632	0.15840
1	1	1	$1e-4$	1	16.7	0.96148	0.92773	565.60429	1.63656
1	1	1	$1e-6$	0.6	66.0	0.20317	0.06447	106.06283	0.09527
1	1	1	$1e-6$	0.8	16.7	0.96148	0.92773	565.60429	1.63656
1	1	1	$1e-6$	1	<u>67.3</u>	0.16662	0.04666	<u>98.05333</u>	0.08452
1	1	1	$1e-6$	2	69.0	<u>0.17601</u>	<u>0.05230</u>	97.61372	<u>0.08688</u>
1	1	1	$1e-6$	3	16.7	0.96148	0.92773	565.60429	1.63656

TABLE VIII
PARAMETER ANALYSIS ON \hat{T}_{min} . THE BEST PERFORMANCES ARE MARKED **BOLD**. THE SECOND BEST PERFORMANCES ARE MARKED UNDERLINED.

\hat{T}_{min}	Errors \uparrow	Errors \downarrow			
	Accuracy (unit in %)	AbsRel	SqRel	RMSE	RMSElog
0	21.0	2.91409	14.15614	1140.67145	0.57624
$1e-3$	32.3	0.83141	1.16434	433.51288	0.27273
$1e-2$	68.3	0.17000	<u>0.05094</u>	93.11345	0.08429
$1e-1$	<u>65.7</u>	<u>0.17235</u>	0.05026	102.81039	<u>0.08727</u>
$2e-1$	<u>65.7</u>	0.17609	0.05288	103.54889	0.08893

and exhaustively conduct experiments to find the suitable set of parameters. Finally, $\lambda_A = \lambda_T = \lambda_{vis} = 1$, $\lambda_D = 0.8$, and $\lambda_{defog} = 1e-6$ are adopted, respectively.

Table VIII and IX show the results under different \hat{T}_{min} and \hat{V}_{max} . We can learn that setting \hat{T}_{min} and \hat{V}_{max} to $1e-2$ and $1e5$ can achieve the best performance, respectively.

D. Ablation studies

In this subsection, we conduct some ablation studies on the loss functions L_{defog} and L_{vis} ; some quantitative results are shown in Table X. We can learn that solely using L_{defog} will improve the performance, while solely using L_{vis} will lead to the non-convergence of the model. However, simultaneously using L_{defog} and L_{vis} leads to the best performance, which proves the effectiveness and necessity of L_{defog} and L_{vis} .

Table XI presents the quantitative comparisons between the proposed model and the naive model; the proposed model integrates the physical laws and the deep learning methods, while the naive model consisting of one Encoder and one Decoder_T directly estimates the visibility map. The naive model is trained with identical configurations and hyperparameters, and RMSE loss is used during training. Moreover, we take the average value of the visibility map as the image-wise estimate. The numbers presented in Table XI demonstrate that the proposed method outperforms the Naive Model by large margins in all metrics.

E. Model complexity

Table XII summarizes the model's time and space complexities. We can learn that the time and space complexities of the proposed method are on a par with other state-of-the-art

TABLE IX

PARAMETER ANALYSIS ON \hat{V}_{max} . THE BEST PERFORMANCES ARE MARKED **BOLD**. THE SECOND BEST PERFORMANCES ARE MARKED UNDERLINED.

\hat{V}_{max}	Errors \uparrow		Errors \downarrow		
	Accuracy (unit in %)	AbsRel	SqRel	RMSE	RMSElog
1e3	53.3	0.19826	0.05809	147.15601	0.10736
1e4	<u>68.0</u>	0.17071	0.05088	94.79418	0.08568
1e5	68.3	0.17000	<u>0.05094</u>	93.11345	0.08429
1e6	68.3	<u>0.17001</u>	<u>0.05094</u>	<u>93.11432</u>	<u>0.08531</u>

TABLE X

ABLATION STUDIES ON LOSS FUNCTION. THE BEST PERFORMANCES ARE MARKED **BOLD**. THE SECOND BEST PERFORMANCES ARE UNDERLINED.

L_{defog}	L_{vis}	Errors \uparrow		Errors \downarrow		
		Accuracy (unit in %)	AbsRel	SqRel	RMSE	RMSElog
-	-	60.0	0.21444	0.08606	109.64792	0.10298
-	\checkmark	16.7	0.96148	0.92773	565.60429	1.63656
\checkmark	-	<u>67.3</u>	<u>0.21279</u>	<u>0.08279</u>	<u>107.93496</u>	<u>0.10204</u>
\checkmark	\checkmark	68.3	0.17000	0.05094	93.11345	0.08429

TABLE XI

QUANTITATIVE RESULTS OF THE VISIBILITY ESTIMATION ON THE FACI DATASET. THE BEST PERFORMANCES AND OUR MODEL ARE MARKED **BOLD**.

Methods	Errors \uparrow		Errors \downarrow		
	Accuracy (unit in %)	AbsRel	SqRel	RMSE	RMSElog
Naive Model	55.3	0.21116	0.06993	143.15237	0.11181
Our	68.3	0.17000	0.05094	93.11345	0.08429

methods. However, the performance of the proposed method outperforms those of state-of-the-art methods by large margins as presented in Table VI.

TABLE XII

MODEL COMPLEXITY. THE TIME COMPLEXITY EVALUATIONS ARE PERFORMED AT AN IMAGE RESOLUTION OF 288×512 ON A SINGLE GEFORCE GTX 1080. TC AND SC REPRESENT TIME AND SPACE COMPLEXITIES, RESPECTIVELY. THE BEST PERFORMANCES AND OUR MODEL ARE MARKED **BOLD**. THE SECOND BEST PERFORMANCES ARE UNDERLINED.

Methods	TC (GFLOPs)	SC (M)
VGG-16 [49]	42.23	134.28
ResNet-50 [43]	12.18	23.52
VisNet [1]	37.92	16.04
Our	<u>14.10</u>	<u>19.30</u>

VI. LIMITATIONS

In this section, the limitations of the proposed model are discussed. Firstly, the method requires the depth map and the transmission map as supervision to train the proposed framework, which may limit the use of the method. Secondly, for the images excluding sky area, the airlight may not be well estimated, further degenerating the performance of the proposed method. We will work on these issues in the future.

VII. CONCLUSION

Visibility estimation under foggy weather is important to traffic safety and transportation infrastructure systems man-

agement. However, most methods mainly adopt professional instruments outfitted at fixed positions on the road to estimate visibility, which is costly and less flexible. Although many trials applying deep learning methods to visibility estimation have been conducted, the estimation accuracy still needs to be improved. Importantly, none of the previous methods considers the uneven fog situations, which occurs frequently in reality, especially in mountain areas.

To mitigate these research gaps, we propose an innovative visibility estimation framework, which integrates deep neural networks and physical law to improve performance. Moreover, we, for the first time, propose a pixel-wise visibility estimation paradigm to take the uneven fog situations into account, which is more informative and practical than a single-valued estimation. Finally, a new virtual dataset, FACI, is collected and proposed for validating the proposed method. Detailed experiments on the FACI dataset and the real-world data demonstrate the effectiveness and practicality of the proposed method. We hope that the proposed method can contribute to the development of intelligent transportation infrastructure systems.

REFERENCES

- [1] A. Palvanov and Y. I. Cho, "Visnet: Deep convolutional neural networks for forecasting atmospheric visibility," *Sensors*, vol. 19, no. 6, p. 1343, 2019.
- [2] Q. Li, S. Tang, X. Peng, and Q. Ma, "A method of visibility detection based on the transfer learning," *Journal of Atmospheric and Oceanic Technology*, vol. 36, no. 10, pp. 1945–1956, 2019.

- [3] S. Rasouli, E. Hariri, and S. Khademi, "Measurement of the atmospheric visibility distance by imaging a linear grating with sinusoidal amplitude and having variable spatial period through the atmosphere," *Journal of the Earth and Space Physics*, vol. 42, no. 2, pp. 449–458, 2016.
- [4] H. Chaabani, F. Kamoun, H. Bargaoui, F. Outay *et al.*, "A neural network approach to visibility range estimation under foggy weather conditions," *Procedia computer science*, vol. 113, pp. 466–471, 2017.
- [5] T. M. Kwon, "Atmospheric visibility measurements using video cameras: Relative visibility," 2004.
- [6] R. Babari, N. Hautiere, E. Dumont, R. Brémond, and N. Paparoditis, "A model-driven approach to estimate atmospheric visibility with ordinary cameras," *Atmospheric Environment*, vol. 45, no. 30, pp. 5316–5324, 2011.
- [7] R. Babari, N. Hautière, E. Dumont, J.-P. Papellard, and N. Paparoditis, "Computer vision for the remote sensing of atmospheric visibility," in *2011 IEEE International Conference on Computer Vision Workshops (ICCV Workshops)*. IEEE, 2011, pp. 219–226.
- [8] X. Cheng, B. Yang, G. Liu, T. Olofsson, and H. Li, "A variational approach to atmospheric visibility estimation in the weather of fog and haze," *Sustainable cities and society*, vol. 39, pp. 215–224, 2018.
- [9] D. Pomerleau, "Visibility estimation from a moving vehicle using the ralph vision system," in *Proceedings of Conference on Intelligent Transportation Systems*. IEEE, 1997, pp. 906–911.
- [10] B. Hamilton, B. Tefft, L. Arnold, and J. Grabowski, "Hidden highways: Fog and traffic crashes on america's roads," 2014.
- [11] D. Fabbian, R. De Dear, and S. Lelleyett, "Application of artificial neural network forecasts to predict fog at canberra international airport," *Weather and forecasting*, vol. 22, no. 2, pp. 372–381, 2007.
- [12] S. B. Costa, F. d. O. Carvalho, R. F. Amorim, A. M. Campos, J. C. Ribeiro, V. N. Carvalho, and D. M. dos Santos, "Fog forecast for the international airport of maceió, brazil using artificial neural network," *Proc. 8th ICSHMO, Foz do Iguacu, Brazil*, pp. 24–28, 2006.
- [13] L. Zhu, G. Zhu, L. Han, N. Wang *et al.*, "The application of deep learning in airport visibility forecast," *Atmospheric and Climate Sciences*, vol. 7, no. 03, p. 314, 2017.
- [14] C. Sakaridis, D. Dai, and L. Van Gool, "Semantic foggy scene understanding with synthetic data," *International Journal of Computer Vision*, vol. 126, no. 9, pp. 973–992, 2018.
- [15] O. Slawinski, J. G. Kowalski, and P. C. Cornillon, "A neural network approach to cloud detection in avhrr images," in *IJCNN-91-Seattle International Joint Conference on Neural Networks*, vol. 1. IEEE, 1991, pp. 283–288.
- [16] N. P. Hyslop, "Impaired visibility: the air pollution people see," *Atmospheric Environment*, vol. 43, no. 1, pp. 182–195, 2009.
- [17] T.-Q. Thach, C.-M. Wong, K.-P. Chan, Y.-K. Chau, Y.-N. Chung, C.-Q. Ou, L. Yang, and A. J. Hedley, "Daily visibility and mortality: assessment of health benefits from improved visibility in hong kong," *Environmental research*, vol. 110, no. 6, pp. 617–623, 2010.
- [18] T. Pejovic, V. A. Williams, R. B. Noland, and R. Toumi, "Factors affecting the frequency and severity of airport weather delays and the implications of climate change for future delays," *Transportation research record*, vol. 2139, no. 1, pp. 97–106, 2009.
- [19] S. J. Dietz, P. Kneringer, G. J. Mayr, and A. Zeileis, "Forecasting low-visibility procedure states with tree-based statistical methods," *Pure and Applied Geophysics*, vol. 176, no. 6, pp. 2631–2644, 2019.
- [20] S. Li, H. Fu, and W.-L. Lo, "Meteorological visibility evaluation on webcam weather image using deep learning features," *Int. J. Comput. Theory Eng*, vol. 9, no. 6, 2017.
- [21] H. Koschmieder, "Theorie der horizontalen sichtweite," *Beitrage zur Physik der freien Atmosphere*, pp. 33–53, 1924.
- [22] A. Palvanov and Y. Im Cho, "Dhcn for visibility estimation in foggy weather conditions," in *2018 Joint 10th International Conference on Soft Computing and Intelligent Systems (SCIS) and 19th International Symposium on Advanced Intelligent Systems (ISIS)*. IEEE, 2018, pp. 240–243.
- [23] Y. You, C. Lu, W. Wang, and C.-K. Tang, "Relative cnn-rnn: Learning relative atmospheric visibility from images," *IEEE Transactions on Image Processing*, vol. 28, no. 1, pp. 45–55, 2018.
- [24] S. Shah, D. Dey, C. Lovett, and A. Kapoor, "Airsim: High-fidelity visual and physical simulation for autonomous vehicles," in *Field and service robotics*. Springer, 2018, pp. 621–635.
- [25] R. Halliwell, M. Matthews, and P. Pisano, "An automated visibility detection algorithm utilizing camera imagery," in *23rd Conference on Interactive Information and Processing Systems for Meteorology, Oceanography, and Hydrology (IIPS)*. Citeseer, 2007.
- [26] L. Xie, A. Chiu, and S. Newsam, "Estimating atmospheric visibility using general-purpose cameras," in *International Symposium on Visual Computing*. Springer, 2008, pp. 356–367.
- [27] J.-J. Liaw, S.-B. Lian, Y.-F. Huang, R.-C. Chen *et al.*, "Using sharpness image with haar function for urban atmospheric visibility measurement," *Aerosol and Air Quality Research*, vol. 10, no. 4, pp. 323–330, 2010.
- [28] R. Babari, N. Hautière, É. Dumont, N. Paparoditis, and J. Misener, "Visibility monitoring using conventional roadside cameras—emerging applications," *Transportation research part C: emerging technologies*, vol. 22, pp. 17–28, 2012.
- [29] K. He, J. Sun, and X. Tang, "Single image haze removal using dark channel prior," *IEEE transactions on pattern analysis and machine intelligence*, vol. 33, no. 12, pp. 2341–2353, 2010.
- [30] W. Wauben and M. Roth, "Exploration of fog detection and visibility estimation from camera images," in *WMO Technical Conference on Meteorological and Environmental Instruments and Methods of Observation, CIMO TECO*, 2016, pp. 1–14.
- [31] X. Cheng, G. Liu, A. Hedman, K. Wang, and H. Li, "Expressway visibility estimation based on image entropy and piecewise stationary time series analysis," *arXiv preprint arXiv:1804.04601*, 2018.
- [32] Q. Li and B. Xie, "Visibility estimation using a single image," in *CCF Chinese Conference on Computer Vision*. Springer, 2017, pp. 343–355.
- [33] A. Pasini and S. Potestà, "Short-range visibility forecast by means of neural-network modelling: a case-study," *Il Nuovo Cimento C*, vol. 18, no. 5, pp. 505–516, 1995.
- [34] K. Wang, H. Zhao, A. Liu, and Z. Bai, "The risk neural network based visibility forecast," in *2009 Fifth International Conference on Natural Computation*, vol. 1. IEEE, 2009, pp. 338–341.
- [35] D. F. Specht *et al.*, "A general regression neural network," *IEEE transactions on neural networks*, vol. 2, no. 6, pp. 568–576, 1991.
- [36] H. Wang, K. Shen, P. Yu, Q. Shi, and H. Ko, "Multimodal deep fusion network for visibility assessment with a small training dataset," *IEEE Access*, vol. 8, pp. 217 057–217 067, 2020.
- [37] S. K. Nayar and S. G. Narasimhan, "Vision in bad weather," in *Proceedings of the Seventh IEEE International Conference on Computer Vision*, vol. 2. IEEE, 1999, pp. 820–827.
- [38] S. G. Narasimhan and S. K. Nayar, "Contrast restoration of weather degraded images," *IEEE transactions on pattern analysis and machine intelligence*, vol. 25, no. 6, pp. 713–724, 2003.
- [39] R. Fattal, "Single image dehazing," *ACM transactions on graphics (TOG)*, vol. 27, no. 3, pp. 1–9, 2008.
- [40] B. Cai, X. Xu, K. Jia, C. Qing, and D. Tao, "Dehazenet: An end-to-end system for single image haze removal," *IEEE Transactions on Image Processing*, vol. 25, no. 11, pp. 5187–5198, 2016.
- [41] M. Ju, Z. Gu, D. Zhang, and H. Qin, "Visibility restoration for single hazy image using dual prior knowledge," *Mathematical Problems in Engineering*, vol. 2017, 2017.
- [42] W. E. K. Middleton, "Vision through the atmosphere," in *Geophysik II/Geophysics II*. Springer, 1957, pp. 254–287.
- [43] K. He, X. Zhang, S. Ren, and J. Sun, "Deep residual learning for image recognition," in *Proceedings of the IEEE conference on computer vision and pattern recognition*, 2016, pp. 770–778.
- [44] C. Godard, O. Mac Aodha, M. Firman, and G. J. Brostow, "Digging into self-supervised monocular depth estimation," in *Proceedings of the IEEE/CVF International Conference on Computer Vision*, 2019, pp. 3828–3838.
- [45] S. Jia, X. Pei, W. Yao, and S. Wong, "Self-supervised depth estimation leveraging global perception and geometric smoothness using on-board videos," *arXiv preprint arXiv:2106.03505*, 2021.
- [46] Z. Wang, A. C. Bovik, H. R. Sheikh, and E. P. Simoncelli, "Image quality assessment: from error visibility to structural similarity," *IEEE transactions on image processing*, vol. 13, no. 4, pp. 600–612, 2004.
- [47] A. Paszke, S. Gross, S. Chintala, G. Chanan, E. Yang, Z. DeVito, Z. Lin, A. Desmaison, L. Antiga, and A. Lerer, "Automatic differentiation in pytorch," 2017.
- [48] D. P. Kingma and J. Ba, "Adam: A method for stochastic optimization," *arXiv preprint arXiv:1412.6980*, 2014.
- [49] K. Simonyan and A. Zisserman, "Very deep convolutional networks for large-scale image recognition," *arXiv preprint arXiv:1409.1556*, 2014.